

Colloidal rod-sphere mixtures: Fluid-fluid interfaces and the Onsager limit

Joseph M. Brader

The James Franck Institute, University of Chicago, 5640 South Ellis Avenue, Chicago, Illinois 60637

Ansgar Esztermann and Matthias Schmidt

Institut für Theoretische Physik II, Heinrich-Heine-Universität Düsseldorf, Universitätsstraße 1, D-40225 Düsseldorf, Germany

(Received 3 May 2002; published 3 September 2002)

Using a geometry-based density functional theory we investigate the free interface between demixed bulk fluid phases of a colloidal mixture of hard spheres and vanishingly thin needles. Results are presented for the spatial and orientational density distributions of the particles, as well as for the interface tension. Density profiles display oscillations on the sphere-rich side of the interface provided the sphere liquid phase is on the oscillatory side of the Fisher-Widom line in the bulk phase diagram. Needles tend to align parallel (perpendicular) to the interface on the needle-rich (sphere-rich) side displaying biaxial (uniaxial) order. Furthermore, we generalize the theory to the Onsager limit for interacting rods, and give explicit expressions for the functional in simple geometries.

DOI: 10.1103/PhysRevE.66.031401

PACS number(s): 82.70.Dd, 61.20.Gy, 64.70.Ja, 61.30.Cz

I. INTRODUCTION

Mixtures of spherical and rodlike particles provide soft matter systems that display astonishingly rich phase behavior [1]. When a second component is added as a depletant agent to a suspension of colloidal spheres, the spheres may exhibit colloidal vapor, liquid, and crystalline phases. Rodlike depletants alone, however, already have rich liquid-crystalline phase behavior. The possible combinations of both types of ordering are vast. Experimental examples of rod-sphere mixtures are dispersions of silica spheres and silica coated bohemite rods [2,3], silica beads immersed in suspensions of rodlike *fd* bacteriophage virus [4], and, in the biological domain, microtubules inside vesicles modeling the eukaryotic cell [5,6]. Experimental work has also been devoted to self-diffusion and sedimentation of spheres in dispersions of rods [7]. Depletion-induced crystallization was found in mixtures of colloidal silica spheres and colloidal silica rods with light microscopy and confocal scanning laser microscopy [3]. Fluid-fluid phase separation was observed experimentally in a mixture of silica spheres and semiflexible polymeric rods [poly(γ -benzyl- α ,L-glutamate) (PBLG) with molecular weight 105 000] [8]. The free interface between demixed fluid phases is one topic that we address in the present work.

As a simple theoretical model of a rod-sphere mixture Bolhuis and Frenkel proposed a binary system of hard spheres and vanishingly thin hard needles [9]. Due to the vanishing needle thickness, and hence the absence of interactions between needles, this system does not display liquid crystalline order, but exhibits (sphere) vapor, liquid, and solid states, as was found in Ref. [9] with simulation and a perturbation theory. The theory is similar to the free volume treatment of the Asakura-Oosawa (AO) model [10,11] of colloidal spheres and noninteracting polymer spheres by Lekkerkerker *et al.* [12]. The depletion potential exerted on a pair of spheres due to the presence of the rods was studied theoretically [13], and experimentally using optical tweezers [4]. Considerable work was done to understand the nature of

the depletion force due to rod-like polymers in the Onsager limit [14], and the interactions between flat plates and between two large spheres via the Derjaguin approximation [15]. Theoretical phase behavior of mixtures of spheres and rods with finite diameter were studied in Ref. [2] and compared to experiment [3], and in a mixture of parallel hard spherocylinders and hard spheres layered phases were investigated [16].

Density-functional theory (DFT) [17,18] is a powerful tool to study equilibrium properties of inhomogeneous many-particle systems. For realistic systems, one usually has to rely on approximations for the central quantity of DFT, the excess free energy functional. One particularly successful example of such an approximation is Rosenfeld's density functional for hard sphere (HS) fluids [19], that also describes the HS solid [20–23]. An early extension of this theory to treat hard convex bodies was proposed [24], and used to derive bulk direct correlation functions for molecular fluids [25], two-dimensional anisotropic fluids [26], and hard sphere chain fluids [27]. The theory of Ref. [24] suffered from an incomplete deconvolution of the Mayer bond leading to an incorrect virial expansion, and an extension to remedy this deficiency was made for the model of hard spheres and hard, vanishingly thin needles [28]. Subsequently, this was also generalized to a hard body amphiphilic mixture [29] and to mixtures of colloidal spheres, rods and polymer spheres [30]. Recently, the entropic torque exerted on a single spherocylinder immersed in a hard sphere fluid at a hard wall was calculated with a similar approach [31].

In contrast to the case of simple fluids, interfaces in such complex systems are genuinely characterized by positional *and* orientational order. Interfaces between phases with different liquid crystalline ordering, like isotropic-nematic interfaces, have attracted considerable interest, see Ref. [32] for a recent study of the hard-rod fluid. In this work, we investigate the free interface between demixed (isotropic) fluid phases in a rod-sphere mixture, an issue that has not been addressed so far. We use the simplest nontrivial model in the context, namely, Bolhuis and Frenkel's mixture of hard

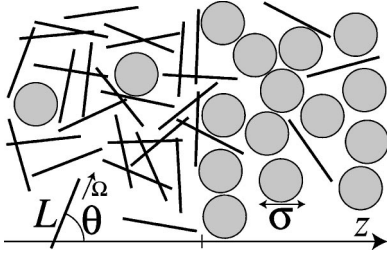


FIG. 1. Model of hard spheres with diameter $\sigma=2R$ and needles with length L . In planar geometry, the z direction is perpendicular to the interface between needle-rich ($z<0$) and sphere-rich ($z>0$) phases. The needle orientation is denoted by Ω , and the angle between Ω and the z axis is θ .

spheres and vanishingly thin needles, and investigate it by means of the geometry-based DFT proposed earlier [28]. As this theory reproduces the bulk fluid free energy and hence the accurate fluid demixing binodal of perturbation theory [9], and was also shown to yield bulk (sphere) pair correlation functions in good agreement with computer simulation results [28], we are confident to apply it to inhomogeneous situations. We find that, driven by packing effects of the spheres, orientational order of the needles occurs at the free fluid-fluid interface, and that the density profiles are oscillatory provided the sphere-rich fluid is on the oscillatory side of the Fisher-Widom line in the bulk phase diagram [33–36]. The interface tension is found to be of the order of the thermal energy per molecular area, and we investigate its scaling with needle length and sphere diameter in detail. Furthermore, we extend the DFT to the case of nonvanishing rod-rod interactions in the Onsager limit and give explicit expressions for the functional in simple geometries.

Similar interface studies using density-functional approaches were recently carried out [37,38] for the AO model [10,11] of colloid-polymer mixtures. Our present model, however, allows us to go beyond those studies through the investigation of orientational order at the interface. Clearly, such ordering is absent in the AO model of spherical bodies.

The paper is organized as follows. In Sec. II we define in more detail the hard sphere-needle mixture for vanishingly thin needles as well as for needles in the Onsager limit. Then we present our DFT approach in Sec. III, generalize it to the Onsager limit and give explicit expressions for the relevant quantities in simple geometries. In Sec. IV, after revisiting the bulk fluid phase behavior, we present results for density and order parameter profiles across the free interface between demixed phases, as well as for the interface tension. We finish with concluding remarks in Sec. V.

II. MODEL

We consider a mixture of hard spheres (species S) with radii R and straight hard needles (species N) with length L and diameter D , see Fig. 1 for a sketch. The spheres interact with a hard core potential $V_{SS}(r)$ as a function of their center separation distance r , which is given by $V_{SS}(r)=\infty$ if $r < 2R$ and zero otherwise. Spheres and needles interact with a hard body interaction that depends, due to the particle

shapes, on the difference vector \mathbf{r} between sphere and needle center, as well as on the needle orientation given by a unit vector Ω pointing along the needle shape. (Hence the needles possess an inflection symmetry, $\Omega \rightarrow -\Omega$.) The sphere-needle interaction is given by $V_{SN}(\mathbf{r}, \Omega) = \infty$ if both shapes overlap, and zero otherwise. In the following, we consider two cases of interactions between needles.

In the first, simpler, case we set $D=0$. Then the needles are noninteracting and $V_{NN}=0$, for all possible distances and orientations. Although these “line” particles would nontrivially collide in a dynamical description, their excluded volume vanishes due to the vanishing particle volume. Hence, configurations of overlapping needles carry vanishing statistical weight. As we are interested in static quantities only, the needles can be regarded as an ideal gas of rotators, solely due to their geometrical properties. As an aside, no such scaling holds in the somewhat similar AO model of hard sphere colloids and ideal (polymer) *spheres*. There the interactions between the particles of the second component are regarded as being ideal from the outset.

In our second case, the needles are treated in the Onsager limit [39], where for thin rods a residual excluded volume persists, leading to nontrivial interaction already in the pure needle system. Again, the pair potential is that of hard bodies and is given, for the difference vector \mathbf{r} between the centers of two needles with orientations Ω and Ω' , as $V_{NN}(\mathbf{r}, \Omega, \Omega') = \infty$ if both rods overlap, and zero otherwise. Note that the Onsager limit is obtained by letting $L/D \rightarrow \infty$ while keeping the combination $\rho_N D L^2$ constant, where ρ_N is the number density of needles. Here we furthermore restrict ourselves to size ratios that fulfill $LD \ll R^2$, hence the sphere surface is assumed to be large compared to the needle surface. This additional restriction is similar in spirit to the Onsager limit for pure needles and constitutes the simplest scaling regime of the three lengths R, L, D . Note that due to the large aspect ratio, there is no need to specify the precise shape of the needle ends, whether, e.g., hemispherical or cylindrical.

We denote the number densities of spheres and needles by $\rho_S(\mathbf{r})$ and $\rho_N(\mathbf{r}, \Omega)$, respectively. As bulk thermodynamic parameters, we use the packing fraction of spheres $\eta = 4\pi R^3 \rho_S / 3$ and the scaled needle density $\rho_* = \rho_N L^2 \sigma$, where $\sigma = 2R$ denotes the sphere diameter. Furthermore, we denote the density in a reservoir of pure needles that is in chemical equilibrium with the system as ρ_N^r and use a scaled version $\rho_*^r = \rho_N^r L^2 \sigma$. The ratio of needle length and sphere diameter, L/σ , and, in our second model, the ratio of needle diameter and length, D/L , are control parameters. As only hard core interactions are present, temperature T is an irrelevant variable that only sets the energy scale through $k_B T$, where k_B is Boltzmann’s constant.

III. DENSITY FUNCTIONAL THEORY

A. Spheres and vanishingly thin needles

In this section, we review briefly the DFT proposed in Ref. [28]. The starting point is a geometrical representation of the particles in terms of weight functions w_μ^i , where i

labels the species, and $\mu=3,2,1,0$ corresponds to the particles' volume, surface, integral mean curvature, and Euler characteristic, respectively [24]. The weight functions are determined to give the Mayer bonds $f_{ij} = \exp(-\beta V_{ij}) - 1$, where $\beta = 1/k_B T$, by a linear combination of terms $w_\gamma^i(\mathbf{r}) * w_{3-\gamma}^j(\mathbf{r})$, where the asterisk denotes the spatial convolution, $g(\mathbf{r}) * h(\mathbf{r}) = \int d^3x g(\mathbf{x}) h(\mathbf{r}-\mathbf{x})$. For needles, following Ref. [24] yields

$$w_1^N(\mathbf{r}, \mathbf{\Omega}) = \frac{1}{4} \int_{-L/2}^{L/2} dl \delta(\mathbf{r} + \mathbf{\Omega}l), \quad (1)$$

$$w_0^N(\mathbf{r}, \mathbf{\Omega}) = \frac{1}{2} [\delta(\mathbf{r} + \mathbf{\Omega}L/2) + \delta(\mathbf{r} - \mathbf{\Omega}L/2)], \quad (2)$$

where $\delta(x)$ is the Dirac distribution. The function w_1^N describes the linear shape of a needle, whereas w_0^N is only nonvanishing at the needle endpoints.

For spheres the weight functions [19,23] are

$$w_3^S(\mathbf{r}) = \Theta(R-r), \quad w_2^S(\mathbf{r}) = \delta(R-r), \quad (3)$$

$$\mathbf{w}_{v2}^S(\mathbf{r}) = w_2^S(\mathbf{r})\mathbf{r}/r, \quad \hat{\mathbf{w}}_{m2}^S(\mathbf{r}) = w_2^S(\mathbf{r})[\mathbf{r}\mathbf{r}/r^2 - \hat{\mathbf{1}}/3], \quad (4)$$

where $r=|\mathbf{r}|$, $\Theta(x)$ is the step function, $\hat{\mathbf{1}}$ is the 3×3 identity matrix, and $\mathbf{r}\mathbf{r}$ is a dyadic product. Further, linearly dependent, weights are $w_1^S(\mathbf{r}) = w_2^S(\mathbf{r})/(4\pi R)$, $\mathbf{w}_{v1}^S(\mathbf{r}) = \mathbf{w}_{v2}^S(\mathbf{r})/(4\pi R)$, $w_0^S(\mathbf{r}) = w_1^S(\mathbf{r})/R$. The weight functions for spheres have different tensorial rank: w_0^S , w_1^S , w_2^S , w_3^S are scalars; \mathbf{w}_{v1}^S , \mathbf{w}_{v2}^S are vectors; $\hat{\mathbf{w}}_{m2}^S$ is a (traceless) second-rank tensor. The Mayer bond between pairs of spheres is obtained through $-f_{SS}/2 = w_3^S * w_0^S + w_2^S * w_1^S - \mathbf{w}_{v2}^S * \mathbf{w}_{v1}^S$ [19]. In order to recover the sphere-needle Mayer bond one uses [28]

$$w_2^{SN}(\mathbf{r}, \mathbf{\Omega}) = 2|\mathbf{w}_{v2}^S(\mathbf{r}) \cdot \mathbf{\Omega}|, \quad (5)$$

which contains information about both species: it is nonvanishing on the surface of a sphere with radius R , but also possesses (needle) orientation dependence. This function allows us to generate the Mayer bond through $-f_{SN}(\mathbf{r}, \mathbf{\Omega}) = w_3^S(\mathbf{r}) * w_0^N(\mathbf{r}, \mathbf{\Omega}) + w_2^{SN}(\mathbf{r}, \mathbf{\Omega}) * w_1^N(\mathbf{r}, \mathbf{\Omega})$, see Appendix A 1 for an explicit calculation. All weight functions are used to obtain weighted densities n_ν^i by smoothing the actual density profiles through spatial convolutions,

$$n_\nu^N(\mathbf{r}, \mathbf{\Omega}) = \rho_N(\mathbf{r}, \mathbf{\Omega}) * w_\nu^N(\mathbf{r}, \mathbf{\Omega}), \quad \nu = 1, 0, \quad (6)$$

$$n_\nu^S(\mathbf{r}) = \rho_S(\mathbf{r}) * w_\nu^S(\mathbf{r}), \quad \nu = 3, 2, 1, 0, v2, v1, m2, \quad (7)$$

$$n_2^{SN}(\mathbf{r}, \mathbf{\Omega}) = \rho_S(\mathbf{r}) * w_2^{SN}(\mathbf{r}, \mathbf{\Omega}). \quad (8)$$

Note that n_ν^N and n_ν^S are ‘‘pure’’ weighted densities, involving only variables of either species [19,23,24]. The function n_2^{SN} is obtained as a convolution of the sphere density with an orientation-dependent weight function; hence it combines characteristics of both species and couples the orientational degrees of freedom of the needles to the sphere distribution.

The (Helmholtz) excess free energy is obtained by integrating over a free energy density,

$$F_{\text{excl}}[\rho_S, \rho_N] = k_B T \int d^3r \int \frac{d^2\Omega}{4\pi} \Phi(\{n_\nu^i\}), \quad (9)$$

where the reduced free energy density Φ is a simple function (not a functional) of the weighted densities n_ν^i . The variable \mathbf{r} runs over space, and as Φ depends also on orientation, $\mathbf{\Omega}$ runs over the unit sphere. The functional form of Φ is obtained by consideration of the exact zero-dimensional excess free energy [28], and is given by

$$\Phi = \Phi_S + \Phi_{SN}, \quad (10)$$

$$\begin{aligned} \Phi_S = & -n_0^S \ln(1 - n_3^S) + (n_1^S n_2^S - \mathbf{n}_{v1}^S \cdot \mathbf{n}_{v2}^S)/(1 - n_3^S) \\ & + [(n_2^S)^3/3 - n_2^S (\mathbf{n}_{v2}^S)^2 + 3(\mathbf{n}_{v2}^S \hat{\mathbf{n}}_{m2}^S \mathbf{n}_{v2}^S \\ & - 3 \det \hat{\mathbf{n}}_{m2}^S)/2]/[8\pi(1 - n_3^S)^2], \end{aligned} \quad (11)$$

$$\Phi_{SN} = -n_0^N \ln(1 - n_3^S) + \frac{n_1^N n_2^{SN}}{1 - n_3^S}. \quad (12)$$

The contribution Φ_S is equal to the pure HS case [19,23], and Φ_{SN} arises from needle-sphere interactions [28]. The arguments of the weighted densities are suppressed in the notation in Eqs. (11, 12); see Eqs. (6–8) for the explicit dependence. This completes the prescription for the excess free energy functional for the case of vanishingly thin needles. For completeness, the ideal free energy is

$$\begin{aligned} F_{\text{id}}[\rho_S, \rho_N] = & \int d^3r \rho_S(\mathbf{r}) \{\ln[\rho_S(\mathbf{r}) \Lambda_S^3] - 1\} \\ & + \int d^3r \int \frac{d^2\Omega}{4\pi} \rho_N(\mathbf{r}, \mathbf{\Omega}) \\ & \times \{\ln[\rho_N(\mathbf{r}, \mathbf{\Omega}) \Lambda_N^3] - 1\}, \end{aligned} \quad (13)$$

where Λ_i is the (irrelevant) thermal wavelength of species $i=S, N$.

B. Spheres and rods in the Onsager limit

In order to deal with rod-rod interactions, we first express the Mayer bond between rods in the Onsager limit through $f_{NN}(\mathbf{r}, \mathbf{\Omega}, \mathbf{\Omega}')/2 = -w_2^{NN}(\mathbf{r}, \mathbf{\Omega}; \mathbf{\Omega}') * w_1^N(\mathbf{r}, \mathbf{\Omega}')$, where w_1^N is defined in Eq. (1), and we introduce

$$w_2^{NN}(\mathbf{r}, \mathbf{\Omega}; \mathbf{\Omega}') = 16D \sqrt{1 - (\mathbf{\Omega} \cdot \mathbf{\Omega}')^2} w_1^N(\mathbf{r}, \mathbf{\Omega}). \quad (14)$$

As a geometrical interpretation, the function w_2^{NN} describes the residual rod surface in the limit of large aspect ratio, see Appendix A 2 for details how the Mayer bond is obtained. We construct an associated weighted density

$$n_2^{NN}(\mathbf{r}, \mathbf{\Omega}') = \int \frac{d^2\Omega}{4\pi} \rho_N(\mathbf{r}, \mathbf{\Omega}) * w_2^{NN}(\mathbf{r}, \mathbf{\Omega}; \mathbf{\Omega}'), \quad (15)$$

where, besides the spatial convolution, an angular convolution is required. This turns out to be necessary for the present case of interacting anisotropic particles. As an aside, we can immediately reformulate the Onsager excess free energy functional for a pure system of rods, being precisely a second order virial expansion, by setting $\Phi = \Phi_{NN}$ in Eq. (9), with

$$\Phi_{NN} = n_1^N n_2^{NN}, \quad (16)$$

where the weighted density n_1^N is given through Eqs. (6) and (1).

For the case of the actual sphere-rod mixture, we insert $\Phi = \Phi_S + \Phi_{SN} + \Phi_{SNN}$ into Eq. (9), where the first two terms are equal to the case of vanishingly thin needles and are given by Eqs. (11) and (12), respectively. The additional contribution due to interactions between rods is found to be

$$\Phi_{SNN} = \frac{n_1^N n_2^{NN}}{1 - n_3^S}, \quad (17)$$

where (as before) the arguments of the weighted densities are suppressed in the notation. This completes the extension of the needle-sphere DFT to interacting rods.

C. Planar geometry

In order to facilitate the application of the theory to situations like the free interface considered below in Secs. IV B, IV C and to planar wall problems, we give explicit expressions for the weight functions in situations depending on a single spatial coordinate z and possessing translational invariance in the x and y directions, where $\mathbf{r} = (x, y, z)$ is a Cartesian coordinate system. Additionally, we assume invariance with respect to rotations around the z axis by an angle φ . The remaining relevant angle θ is that between an orientation $\mathbf{\Omega}$ and the z axis, see Fig. 1. Hence $\rho_S(\mathbf{r}) = \rho_S(z)$, and $\rho_N(\mathbf{r}, \mathbf{\Omega}) = \rho_N(z, \theta)$. Considering $\theta \in [0, \pi/2]$ is sufficient, due to the inflection symmetry of the needles. In this *planar geometry* the weighted densities, Eqs. (6)–(8) and (15), can be expressed as

$$n_v^N(z, \theta) = \int dz' \rho_N(z', \theta) w_v^N(z - z', \theta), \quad (18)$$

$$n_v^S(z) = \int dz' \rho_S(z') w_v^S(z - z'), \quad (19)$$

$$n_2^{SN}(z, \theta) = \int dz' \rho_S(z') w_2^{SN}(z - z', \theta), \quad (20)$$

$$n_2^{NN}(z, \theta) = \int dz' \int_0^\pi d\theta' \rho_N(z', \theta') w_2^{NN}(z - z', \theta'; \theta), \quad (21)$$

where the effective weight functions $w_v^N(z, \theta)$, $w_v^S(z)$, $w_2^{SN}(z, \theta)$ are obtained by carrying out the integrations in Eqs. (6)–(8) and (15) over coordinates x, y , see Appendix B for the details. Explicitly, for the needles one obtains

$$w_1^N(z, \theta) = (4 \cos \theta)^{-1} \Theta \left(\frac{L}{2} \cos \theta - |z| \right), \quad (22)$$

$$w_0^N(z, \theta) = \frac{1}{2} \delta \left(\frac{L}{2} \cos \theta - |z| \right). \quad (23)$$

For the spheres

$$w_3^S(z) = \pi(R^2 - z^2) \Theta(R - |z|), \quad (24)$$

$$w_2^S(z) = 2\pi R \Theta(R - |z|), \quad (25)$$

$$w_{v2}^S(z) = 2\pi z \Theta(R - |z|) \mathbf{e}_z, \quad (26)$$

$$\hat{w}_{m2}^S(z) = \pi \left(\frac{z^2}{R} - \frac{R}{3} \right) \Theta(R - |z|) \text{diag}(-1, -1, 2), \quad (27)$$

where \mathbf{e}_z is the unit vector pointing along the z axis and $\text{diag}(\cdot)$ denotes a 3×3 diagonal matrix. The linearly dependent weight functions are $w_1^S(z) = \Theta(R - |z|)/2$, $w_0^S(z) = \Theta(R - |z|)/(2R)$, $w_{v1}^S(z) = z \Theta(R - |z|) \mathbf{e}_z/(2R)$. The mixed weight function is obtained as

$$w_2^{SN}(z, \theta) = \begin{cases} 8 \sqrt{R^2 \sin^2 \theta - z^2} \\ + 8z \cos \theta \\ \times \arcsin \left(\frac{z \cot(\theta)}{\sqrt{R^2 - z^2}} \right) & \text{if } |z| < R \sin \theta, \\ 4\pi |z| \cos \theta & \text{if } R \sin \theta \leq |z| \leq R, \\ 0 & \text{otherwise.} \end{cases} \quad (28)$$

For the case of nonvanishing rod-rod interactions (Sec. III B), the additional weight function can be obtained up to a quadrature as

$$w_2^{NN}(z, \theta; \theta') = \frac{D \tan \theta}{\pi} \Theta \left(\frac{L \cos \theta}{2} - |z| \right) \int_0^{2\pi} d\varphi \\ \times \sqrt{1 - (\sin \theta' \sin \theta \cos \varphi + \cos \theta' \cos \theta)^2}. \quad (29)$$

This fully specifies the DFT in planar geometry. We note that the tensorial weight function, Eq. (27), is included for reasons of completeness. Albeit being crucial for a reliable description of the solid [23], it is known to yield a small contribution to the free energy in planar geometry, and may be neglected to a good approximation. Below in Sec. IV we will adopt this strategy.

D. Spherical geometry

Here we focus on situations that only depend on the distance to the origin, r , and that remain invariant under rotations around the origin. This is realized, e.g., in the important test-particle limit that allows us to obtain pair distribution functions by minimizing the functional in the presence of a test sphere fixed at the origin. In spherical geometry, only the

angle θ between needle orientation $\mathbf{\Omega}$ and position \mathbf{r} remains relevant, and $\rho_S(\mathbf{r}) = \rho_S(r)$, and $\rho_N(\mathbf{r}, \mathbf{\Omega}) = \rho_N(r, \theta)$. Again, we can restrict to $0 \leq \theta \leq \pi/2$. The pure weighted densities, Eqs. (6)–(8) can be expressed as

$$n_v^N(r, \theta) = \int_0^\infty dr' \rho_N(r', \theta) w_v^N(r, r', \theta), \quad (30)$$

$$n_v^S(r) = \int_0^\infty dr' \rho_S(r') w_v^S(r, r'), \quad (31)$$

where the reduced weight functions are

$$w_1^N(r, r', \theta) = \frac{r'}{4\sqrt{r'^2 - r^2 \sin^2 \theta}} \times \sum_{\pm} \Theta\left(\frac{L}{2} - |r \cos \theta \pm \sqrt{r'^2 - r^2 \sin^2 \theta}|\right), \quad (32)$$

$$w_0^N(r, r', \theta) = \frac{1}{2} \sum_{\pm} \delta\left(r' - \sqrt{\left(r \pm \frac{L}{2} \cos \theta\right)^2 + \frac{L^2}{4} \sin^2 \theta}\right), \quad (33)$$

$$w_3^S(r, r') = \frac{\pi r'}{r} [R^2 - (r - r')^2] \Theta(R - |r - r'|), \quad (34)$$

$$w_2^S(r, r') = \frac{2\pi R r'}{r} [\Theta(R - |r - r'|) - \Theta(R - r - r')], \quad (35)$$

$$\mathbf{w}_{v2}^S(r, r') = \frac{R^2 + r^2 - r'^2}{2Rr} w_2^S(r, r') \frac{\mathbf{r}}{r}, \quad (36)$$

$$\hat{\mathbf{w}}_{m2}^S(r, r') = \frac{1}{2} \left[\left(\frac{R^2 + r^2 - r'^2}{2Rr} \right)^2 - \frac{1}{3} \right] w_2^S(r, r') \left(3 \frac{\mathbf{r}\mathbf{r}}{r^2} - \hat{\mathbf{1}} \right). \quad (37)$$

In Eqs. (36), (37) only the dependence on the scalar argument r is important; the dependence on \mathbf{r}/r is trivial due to the structure of Φ , Eq. (11). The linearly dependent weight functions are $w_1^S(r, r') = r'/(2r)[\Theta(R - |r - r'|) - \Theta(R - r - r')]$, $w_{v1}^S(r, r') = (r^2 - r'^2 + R^2)/(2Rr)w_1^S(r, r')$, $w_0^S(r, r') = r'/(2Rr)[\Theta(R - |r - r'|) - \Theta(R - r - r')]$. The mixed weight function is

$$w_2^{SN}(r, r', \theta) = \begin{cases} \frac{8r'}{r} \left[\sqrt{r'^2(1-u^2) - R^2 \cos^2 \theta} + (r - r'u) \cos(\theta) \right. \\ \quad \left. \times \arcsin\left(\frac{(r - r'u) \cot \theta}{r' \sqrt{1-u^2}}\right) \right] & \text{if } |r - r'u| < r' \sqrt{1-u^2} \tan \theta, \\ 4\pi(r'/r)|r - r'u| \cos \theta & \text{if } |r - r'u| \geq r' \sqrt{1-u^2} \tan \theta, \\ 0 & \text{if } |u| \geq 1, \end{cases} \quad (38)$$

where $u = (r'^2 + r^2 - R^2)/(2rr')$. For the remaining needle weight w_2^{NN} we could not obtain simple analytic expressions; a full numerical calculation is required to obtain n_2^{NN} .

We note that for a test-particle limit calculation, where a hard sphere is fixed at the origin, the above expression can be simplified, as the density distributions vanish inside the test particle. This allows us to omit the second step function in Eq. (35) and rewrite the convolution kernels for spheres as a function of the difference $r - r'$ only. The expressions given above are completely general, hence apply also to cases of nonvanishing densities in the immediate vicinity of the origin.

IV. RESULTS

A. Bulk phase diagram

As a prerequisite for our interface study, we reconsider the bulk fluid demixing phase diagram of hard spheres and

vanishingly thin needles. Within our approach, this is obtained from the bulk Helmholtz free energy, which in turn is obtained by applying the density functional (outlined in Sec. III A) to constant density fields of spheres and needles. Then, the weighted densities become proportional to the respective bulk densities, $n_v^i = \xi_v^i \rho_i$, where the proportionality constants are fundamental measures given by $\xi_v^i = \int d^3x w_v^i$. For spheres $\xi_3^S = 4\pi R^3/3$, $\xi_2^S = \xi_2^{SN} = 4\pi R^2$, $\xi_1^S = R$, $\xi_0^S = 1$, whereas for needles $\xi_1^N = L/4$, $\xi_0^N = 1$. Then the excess Helmholtz free energy per volume V is given by $F_{\text{exc}}(\rho_S, \rho_N)/V = \phi_{\text{HS}}(\rho_S) - \rho_N k_B T \ln \alpha(\rho_S)$, where $\phi_{\text{HS}}(\rho_S)$ is the excess free energy density of pure hard spheres in the scaled-particle (and Percus-Yevick compressibility) approximation and $\alpha = (1 - \eta) \exp[-(3/2)(L/\sigma)\eta/(1 - \eta)]$. This expression for the free energy is identical to the result from the perturbation theory of Bolhuis and Frenkel [9]. We note that this is also equivalent to a straightforward application of scaled-particle theory for nonspherical bodies [40] to the current model.

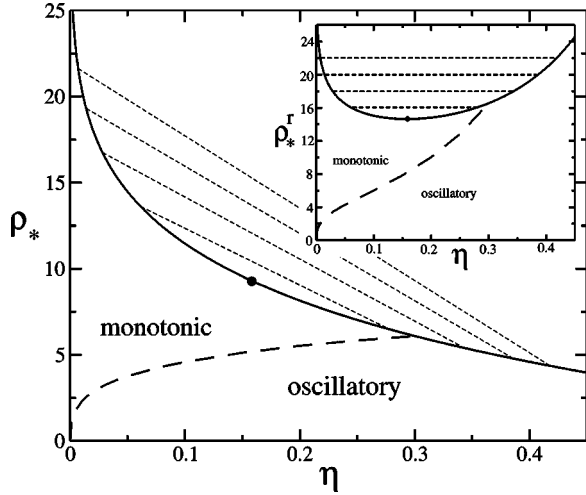


FIG. 2. Fluid-fluid demixing phase diagram of the mixture of hard spheres and vanishingly thin needles with size ratio $L/\sigma=1$ obtained from DFT. Shown are the binodal (solid line) and the Fisher-Widom line (dashed) dividing states where the ultimate decay of correlation functions is either monotonic or damped oscillatory. Tielines (short-dashed) between coexisting states are shown for $\rho_*^r = 16, 18, 20, 22$. The main plot uses system representation with η and ρ_* ; the inset is in reservoir representation with η and ρ_*^r .

From the free energy all thermodynamic quantities can be calculated, and equating the total pressure and the chemical potentials of both species in both phases yields the coexisting densities. The resulting binodal was found to be in remarkable agreement with simulation results [9].

Here we consider the case of equal sphere diameter and needle length, $\sigma=L$, where fluid-fluid phase separation is stable with respect to freezing [9] and display the phase diagram in system representation (as a function of η and ρ_*) in Fig. 2. Shown is the binodal for coexisting states, where a sphere-rich and needle-poor fluid (sphere liquid) coexists with a sphere-poor and needle-rich fluid (sphere gas). For low densities, the density discontinuity vanishes at a critical point. We also display the Fisher-Widom (FW) line, which separates regimes in the phase diagram where the ultimate decay of pair correlation functions (and inhomogeneous one-body density profiles) at large separation is either damped oscillatory or monotonic [33–36]. The FW line was calculated for the present model in Ref. [28] by considering the poles of the partial structure factors in the plane of complex wave vectors [34,35]. Furthermore, we display four tielines between coexisting fluid states. These belong to reservoir densities of needles $\rho_*^r = 16, 18, 20, 22$, and indicate the states where we will carry out detailed structural studies below. Tielines are horizontal in the phase diagram in needle reservoir representation (as a function of η and ρ_*^r), see the inset in Fig. 2. The smallest reservoir density, $\rho_*^r = 16$, is close to the critical point (which is located at $\eta=0.15767$, $\rho_* = 9.3141$, $\rho_*^r = 14.642$). For $\rho_*^r = 16$ the liquid density is located well on the monotonic side of the FW line, hence we expect one-body interface profiles to decay monotonically into both bulk phases. The set of the three higher reservoir densities ($\rho_*^r = 18, 20, 22$) covers the region up to the triple

point, which was located with perturbation theory at $\rho_*^r \approx 24$ [9]. For these states we expect damped oscillatory profiles on the sphere-rich side of the interface.

Before turning to the fluid-fluid interface, we summarize the bulk properties of spheres and rods in the Onsager limit in bulk given in Sec. III B. In an isotropic state, we find that $n_2^{NN} = \xi_\nu^{NN} \rho_N$, where $\xi_\nu^{NN} = \pi L D$ equals the leading contribution to the surface of a rod in the limit $L/D \rightarrow \infty$. It follows that the additional contribution to the free energy density due to rod-rod interactions is $(\pi/4) \rho_N^2 L^2 D / (1 - \eta)$, which is identical to the result from scaled-particle theory [40]. We leave a more detailed investigation of the phase behavior to possible future work.

B. Structure of the fluid-fluid interface

Here and in the following we restrict ourselves to the simple case of spheres mixed with vanishingly thin needles, and aim at an understanding of the free interface between demixed fluid states, see Fig. 1 for a schematic sketch of the following situation: Two demixed bulk fluids are in equilibrium in contact; the coordinate perpendicular to their (planar) interface is denoted by z , and the sphere-poor (-rich) phase is present for negative (positive) z values. The coordinate origin (in z) is set to the position of the Gibbs dividing surface, hence the z -coordinate fulfills $\int_{-\infty}^0 dz [\rho_S(z) - \rho_S(-\infty)] + \int_0^{\infty} dz [\rho_S(z) - \rho_S(\infty)] = 0$. Note that as we deal with isotropic states for $z \rightarrow \pm \infty$, the planar geometry considered in Sec. III C applies.

The numerical minimization of the density functional of Sec. III A is done by an iteration technique, see, e.g., [41]. We discretize $\rho_S(z)$ and $\rho_N(z, \theta)$ in z direction with a resolution of 0.01σ , and we find that angular discretization in 20–50 steps is sufficient to get reliable results for density profiles. For the calculation of interface tensions between demixed fluids (Sec. IV C), we use 120 steps. Note that when, say, 20 needle orientations are considered, we are dealing in effect (due to the additional sphere profile) with a 21 component mixture.

We chose the size ratio $\sigma/L=1$ for our interface study. This is of the same order as realized in the experiments [8] with silica spheres of 78 nm diameter and polymer rods (PBLG) with $L=70$ nm. However, we disregard effects arising from rod flexibility and finite rod thickness and hence consider only $D=0$ (note that $D=1.6$ nm for the polymer in [8]). We first turn to the sphere density profiles, $\rho_S(z)$, displayed in Fig. 3 as a function of the scaled distance z/σ for scaled needle reservoir densities $\rho_*^r = 16, 18, 20, 22$. These statepoints are indicated by tielines in Fig. 2. The asymptotic densities for $z \rightarrow \pm \infty$ in Fig. 3 correspond (up to the factor $\pi/6$) to the sphere packing fractions at both ends of the tielines. With increasing ρ_*^r , and hence increasing distance to the critical point, the interface becomes sharper, i.e., it crosses over from one to the other limiting (bulk) value over a shorter distance. For the highest needle reservoir density considered, $\rho_*^r = 22$, clear oscillations emerge on the liquid side of the interface, see the inset in Fig. 3. The amplitude of the oscillations, however, is considerably smaller than that typically found at interfaces in the AO model (where the

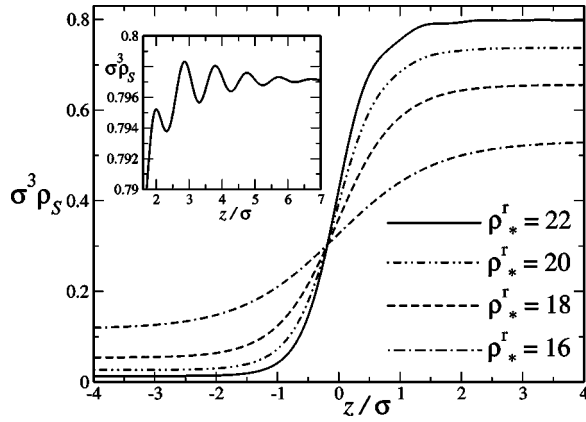


FIG. 3. Scaled sphere density profiles $\sigma^3 \rho_S(z)$ at the free interface between sphere-poor ($z < 0$) and sphere-rich ($z > 0$) phases as a function of the scaled distance z/σ perpendicular to the interface for $\rho_*^r = 16, 18, 20, 22$ corresponding to the tielines in the phase diagram, Fig. 2. The inset shows a magnified view of the (oscillatory) profile $\sigma^3 \rho_S(z)$ as a function of z/σ at the sphere-rich side for $\rho_*^r = 22$.

depletants are ideal spheres rather than needles) [37]. From the general theory of asymptotic decay of correlation functions [34,35], we expect that all statepoints where the liquid density is inside the oscillatory region of the phase diagram (separated by the FW line) will display similar behavior, and indeed we find oscillations on the liquid side of the interface also for $\rho_*^r = 18, 20$. The liquid state at density $\rho_*^r = 16$ is inside the monotonic region, and no oscillations emerge upon magnifying the corresponding density profile in Fig. 3.

In the present geometry, the needle density profile depends on two variables, namely, the perpendicular distance z from the interface and the angle θ of needle orientation and interface normal. The DFT yields $\rho_N(z, \theta)$ fully dependent on both variables. In order to demonstrate this, we chose $\rho_*^r = 22$ as an example and display in Fig. 4 $\rho_*(z, \theta) \sin \theta$ as

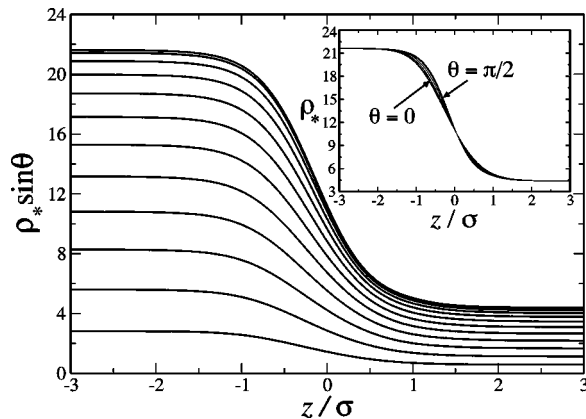


FIG. 4. Scaled needle density multiplied by the spherical volume element, $\rho_*(z, \theta) \sin \theta$, as a function of z/σ at the interface between sphere-poor ($z < 0$) and sphere-rich ($z > 0$) fluids for $\rho_*^r = 22$. Each curve is for fixed angle θ to the interface normal; from bottom to top θ increases from 0 (direction normal to the interface) to $\pi/2$ (direction parallel to the interface) in steps of $\pi/24$. The inset shows the bare $\rho_*(z, \theta)$ without the volume element $\sin \theta$.

a function of z/σ . The factor $\sin \theta$ is the spherical volume element, hence the density distribution at a given angle θ is weighted according to the actual probability that θ is attained. This weight is maximal for $\theta = \pi/2$ (parallel to the interface) and vanishes for $\theta = 0$ (perpendicular to the interface). In order to graphically represent the density profile, we display a set of curves parametrized by θ ; each curve then depends on the single variable z , see Fig. 4. As expected, the needles show a clear tendency to aggregate on the sphere-poor side of the interface. In order to assess the orientational distribution we also plot the bare $\rho_*(z, \theta)$ in the inset of Fig. 4. We observe that for fixed z on the needle-rich side of the profiles the density increases with increasing θ . This means that large angles are favored, hence the needles tend to arrange parallel to the surface, corresponding to biaxial order. On the needle rich side of the interface, however, the opposite trend is manifest. Upon increasing θ at fixed z the density decreases. Hence small angles are more favorable; needles arrange perpendicular to the interface displaying uniaxial order.

In order to investigate the needle behavior in more detail, we obtain two characteristic distributions from the full needle density profile $\rho_*(z, \theta)$. One is the orientation averaged needle density profile, defined as

$$\bar{\rho}_N(z) = \int \frac{d^2 \Omega}{4\pi} \rho_N(\mathbf{r}, \Omega), \quad (39)$$

$$= \frac{1}{2} \int_0^{\pi/2} d\theta \sin(\theta) \rho_N(z, \theta), \quad (40)$$

which measures the density of needle midpoints regardless of their orientation. The other is an orientational order parameter profile defined as

$$\langle P_2(\cos \theta) \rangle = \bar{\rho}_N(z)^{-1} \int \frac{d^2 \Omega}{4\pi} \rho_N(\mathbf{r}, \Omega) P_2(\cos \theta), \quad (41)$$

$$= [2\bar{\rho}_N(z)]^{-1} \int d\theta \sin(\theta) \rho_N(z, \theta) P_2(\cos \theta), \quad (42)$$

where $P_2(x) = (3x^2 - 1)/2$ is the second Legendre polynomial. Negative values of $\langle P_2(\cos \theta) \rangle$ indicate biaxial ordering, the extreme value being $-1/2$ for full parallel alignment to the interface (needles with $\theta = \pi/2$ lying in a plane). Positive values $\langle P_2(\cos \theta) \rangle$ indicate uniaxial ordering, the extreme value (unity) is attained for perpendicular alignment to the interface ($\theta = 0$). Finally, $\langle P_2(\cos \theta) \rangle = 0$ indicates isotropic states. Note that this order parameter has the same inflection symmetry as the needles.

In Fig. 5 we show $\bar{\rho}_N(z)$ for the four statepoints considered. A crossover from high values for negative z to low values for positive z is manifest; hence, as observed before, the needles are depleted in the space occupied by the colloids. The inset in Fig. 5 shows a magnified view of the profile for $\rho_*^r = 22$ on the sphere-rich side of the interface.

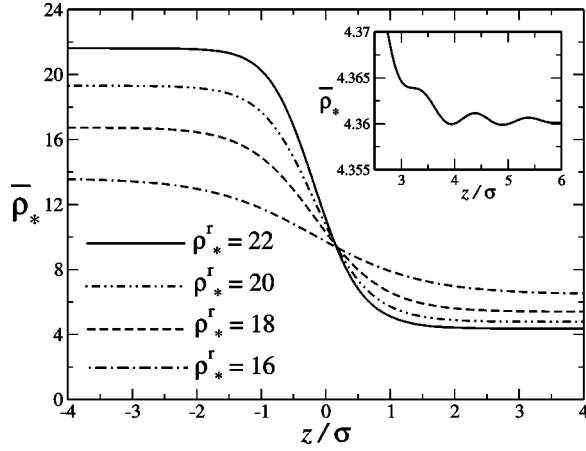


FIG. 5. Orientation averaged needle density profiles $\bar{\rho}_*(z)$ as a function of the scaled distance z/σ for $\rho_*^r = 16, 18, 20, 22$ corresponding to Fig. 3. The inset shows $\bar{\rho}_*(z)$ as a function of z/σ on the sphere-rich side ($z > 0$) of the interface for $\rho_*^r = 22$. Damped oscillations are visible.

Clear oscillations can be observed. These arise from the packing effects of the *spheres*, and are “imprinted” on the needle distribution.

We next turn to the order parameter profile $\langle P_2(\cos \theta) \rangle$, see Fig. 6. On the needle-rich side ($z < 0$) of the interface we find that $\langle P_2(\cos \theta) \rangle < 0$. This indicates needle ordering parallel to the interface, and can be understood in terms of packing effect, similar to those of rods near a hard wall. On the sphere-rich side ($z > 0$) we find that $\langle P_2(\cos \theta) \rangle > 0$, hence the needles are oriented preferentially perpendicular to the interface. We attribute the ordering to needles that stick through the voids in the first sphere layer.

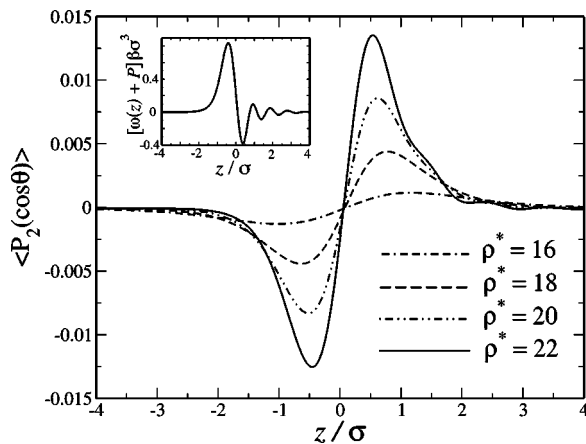


FIG. 6. Orientational order parameter profiles $\langle P_2(\cos \theta) \rangle$ as a function of the scaled distance z/σ for $\rho_*^r = 16, 18, 20, 22$ across the interface between sphere-poor ($z < 0$) and sphere-rich ($z > 0$) fluids. Negative values indicate parallel, positive values indicate normal alignment of needles relative to the interface. The inset shows the (scaled) integrand of the interface tension, $[\omega(z) + P]\beta\sigma^3$ as a function of z/σ for $\rho_*^r = 22$.

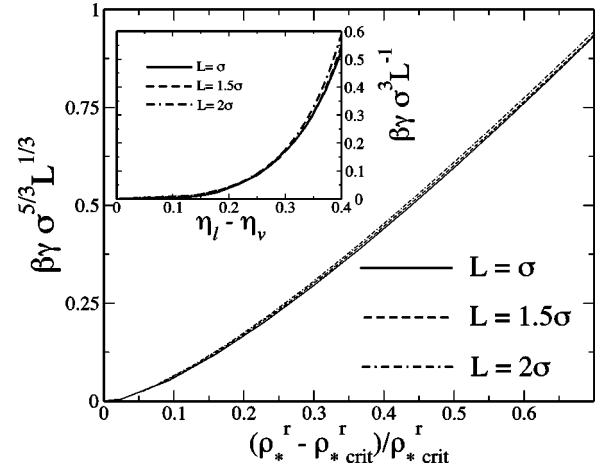


FIG. 7. Scaled interface tension $\beta\gamma\sigma^{5/3}L^{1/3}$ as a function of the scaled distance from the critical point $(\rho_*^r - \rho_{*crit}^r)/\rho_{*crit}^r$ for size ratios $L/\sigma = 1, 1.5, 2$. All curves practically collapse onto each other. The inset shows the scaled interface tension $\beta\gamma\sigma^3L^{-1}$ as a function of the difference between liquid and vapor sphere packing fractions, $\eta_l - \eta_v$, for the same size ratios $L/\sigma = 1, 1.5, 2$.

C. Interface tension

The interface tension γ between demixed fluids is defined as the difference per unit area in grand potentials in the inhomogeneous situation and in bulk. It is given by

$$\gamma A = \bar{\Omega} + PV, \quad (43)$$

where A is the interface area, $\bar{\Omega}$ is the grand potential in the inhomogeneous situation, and P is the total pressure. Within our DFT approach it is obtained from

$$\gamma = \int dz [\omega(z) + P], \quad (44)$$

$$\omega(z) = -\mu_S \rho_S(z) - \mu_N \bar{\rho}_N(z) + \beta \int \frac{d^2 \Omega}{4\pi} \Phi(\{n_v^i(z, \theta)\}), \quad (45)$$

where Φ is the excess free energy density [given through Eqs. (10–12)] dependent on the weighted densities n_v^i [Eqs. (18–20)], and μ_i is the chemical potential of species $i = S, N$. From dimensional analysis, it is clear that the typical scale of γ should be the thermal energy, $k_B T$, divided by an area that is related to molecular length scales. However, as we deal with a binary mixture it is not obvious which power b in $L^b \sigma^{2-b}$ gives the correct scaling with varying size ratio L/σ . We restrict ourselves to the cases $L/\sigma = 1, 1.5, 2$, where we find that $b = 1/3$ gives an almost complete data collapse, see Fig. 7 for a plot of $\beta\gamma\sigma^{5/3}L^{1/3}$ as a function of the scaled distance to the critical value of the needle reservoir density, $(\rho_*^r - \rho_{*crit}^r)/\rho_{*crit}^r$. For states close to the critical point, we find mean-field scaling of the surface tension, $\gamma \propto (\rho_*^r - \rho_{*crit}^r)^{3/2}$. For $(\rho_*^r - \rho_{*crit}^r)/\rho_{*crit}^r > 0.4$ a linear relation is found that extends up to the triple point, for $L = \sigma$ this is from the perturbation theory of Ref. [9] roughly at the right end of the horizontal axis in Fig. 7.

The magnitude of the interface tension is mainly governed by the difference in bulk densities of both phases. Hence a relevant variable is the difference $\eta_l - \eta_v$, where η_l (η_v) is the sphere packing fraction in the coexisting liquid (vapor) phase. In the same spirit as above, we seek a combination of length scales to scale $\beta\gamma$, in order to obtain data collapse for different L/σ . It turns out that this is the case for $\beta\gamma\sigma^3L^{-1}$, see the inset in Fig. 7. Clearly, the different exponent to the case above arises from the relation between η and ρ_* given through the binodals for different L/σ . Although we only present results for $\sigma \leq L \leq 2\sigma$, we expect the scaling relations to hold beyond that range. However, for $L \gg \sigma$ there might well be a crossover to a different scaling regime, and preliminary results show deviations already for $L = 5\sigma$.

As a final issue, we seek to elucidate further the origin of the surface tension. A recent study by Archer and Evans addressed this issue in a binary mixture of Gaussian core particles [42] (see Figs. 11 and 12 therein). They consider two different regimes for their model: (a) where demixing is driven by nonadditivity and (b) where it is driven by energetics, and construct two new variables, namely the total density and a local concentration. In order to calculate the surface tension one must perform the integral Eq. (22) in Ref. [42] [corresponding to our Eq. (44)]. If the integrand is plotted they find that in regime (a) it closely resembles the local concentration and in regime (b) the total density. Their conclusion is that, in one regime, γ is dominated by concentration fluctuations and, in the other, by fluctuations in the total density.

Applying this analysis to our model, we find that neither local concentration nor total density resembles the integrand of the surface tension in Eq. (44). However, the integrand closely resembles the (negative) of the orientational order parameter, see the inset in Fig. 6 for a plot of $[w(z) + P]\beta\sigma^3$ as a function of z/σ for the largest reservoir density considered, $\rho_*^r = 22$. As interpretation of the similarity, negative values of $\langle P_2(\cos \theta) \rangle$ indicate a loss of rotational entropy, and hence a positive contribution to γ . Positive values of $\langle P_2(\cos \theta) \rangle$ indicate a relaxation of the needles sticking through the first sphere layer and hence lowering the tension. From this analysis, it is tempting to argue that in the present model the surface tension is determined by *orientation* fluctuations.

V. CONCLUSIONS

In conclusion, we have considered the free (planar) interface between demixed fluid phases in a model mixture of spherical and needle-shaped colloidal particles. We focused on the case of vanishingly thin needles, which constitutes a minimal model for orientational order at fluid interfaces. Both sphere and needle density profiles show either monotonic or damped oscillatory behavior on the sphere-rich (and needle-poor) side of the interface, depending on which side of the Fisher-Widom line in the bulk phase diagram the sphere liquid state resides. The amplitude of the oscillations, however, is considerably smaller than in the related AO model of spherical (polymer) depletants, and will be further reduced by capillary fluctuations that are not taken into ac-

count in the present treatment. It is tempting to interpret the smaller amplitude in the current model by a washing out of oscillations due to the depletants' rotator degrees of freedom, which are absent in the AO case. On the needle-rich (and sphere-poor) side of the interface both density profiles decay monotonically towards the respective bulk densities. Needles possess biaxial order on the needle-rich side, i.e., they lie preferentially parallel to the interface plane. This can be understood in terms of simple packing of needles against the dense hard sphere fluid. On the sphere-rich side uniaxial order of needles occurs, i.e., needles tend to be oriented normal to the interface. This is somewhat surprising, and we interpret this effect as being caused by the void structure of the hard sphere fluid, into which the needles stick to maximize their entropy.

We have furthermore shown that the geometry-based DFT can be consistently extended to the case of hard spheres mixed with interacting rods in the Onsager limit. The extensions of geometry-based DFT in Ref. [28] are the integration over director space [Eq. (9)], and the introduction of double-indexed weight functions [Eq. (5)] are supplemented in this work by the introduction of angular convolutions [Eq. (15)] to obtain weighted densities. The consistent treatment of nontrivial rod-rod interactions provides an important stepping stone towards the treatment of more general hard body systems. We have given explicit expressions for the present density functional for the important cases of planar and spherical symmetries, facilitating future studies.

We emphasize that testing our predictions for the fluid-fluid interface constitutes a demanding task for computer simulations due to the large numbers of needles involved at state points of interest, and due to the difficulty of stabilizing the free fluid-fluid interface in a finite simulation box. An alternative to circumvent the first problem could be to study an effective one-component system of spheres that interacts by means of the needle-depletion potential [13], although, such an approach would prevent study of the orientational distribution of the needles.

ACKNOWLEDGMENTS

We thank R. Evans, D. Oxtoby, H. Löwen, G. A. Vliegthart, and C. Bechinger for useful discussions. The work of J.M.B. was supported by the National Science Foundation (through Grant No. CHE9800074 and the NSF Materials Research Science and Engineering Center at the University of Chicago).

APPENDIX A: DECONVOLUTION OF MAYER BONDS

1. The sphere-needle Mayer bond

We take the difference vector between the centers of mass of needle and sphere to lie in the equatorial plane: $\mathbf{r} = (r \sin \varphi, r \cos \varphi, 0)$. Due to the rotational symmetry, we can choose the needle to be aligned parallel to the y axis: $\boldsymbol{\Omega} = (0, 1, 0)$. Then

$$w_3^S(\mathbf{r}) * w_0^N(\mathbf{r}, \mathbf{\Omega}) = \frac{1}{2} \int_0^\infty dr' \int_0^{2\pi} d\varphi' \int_0^\pi d\theta' r'^2 \sin \theta' \Theta(R-r') \sum_{\pm} \delta(r \sin \varphi - r' \sin \theta' \sin \varphi') \\ \times \delta\left(r \cos \varphi - r' \sin \theta' \cos \varphi' \pm \frac{L}{2}\right) \delta(-r' \cos \theta') \quad (\text{A1})$$

$$= \frac{1}{2} \sum_{\pm} \Theta\left(R^2 - r^2 - \frac{L^2}{4} \pm Lr \cos \varphi\right), \quad (\text{A2})$$

and

$$w_2^{SN}(\mathbf{r}, \mathbf{\Omega}) * w_1^N(\mathbf{r}, \mathbf{\Omega}) = \frac{1}{2} \int_0^\infty dr' \int_0^{2\pi} d\varphi' \int_0^\pi d\theta' r'^2 \sin \theta' \left| \begin{pmatrix} \sin \theta' \sin \varphi' \\ \sin \theta' \cos \varphi' \\ \cos \theta' \end{pmatrix} \cdot \begin{pmatrix} 0 \\ 1 \\ 0 \end{pmatrix} \right| \delta(R-r') \\ \times \int_{-L/2}^{L/2} dl \delta(r \sin \varphi - r' \sin \theta' \sin \varphi') \delta(r \cos \varphi - r' \sin \theta' \cos \varphi' + l) \delta(-r' \cos \theta') \quad (\text{A3})$$

$$= \frac{1}{2} \sum_{\pm} \Theta(R - |r \sin \varphi|) \Theta\left(\frac{L}{2} - \left| r \cos \varphi \pm \sqrt{R^2 - r^2 \sin^2 \varphi} \right|\right), \quad (\text{A4})$$

where the integrals over θ' , r' , and l in Eqs. (A1), (A3) are straightforward. The integral over φ is split into two domains: for $0 < \varphi < \pi$, $\sin \varphi$ is positive, while for $\pi < \varphi < 2\pi$ it is negative. The sum of Eqs. (A2), (A4) represents the (negative) Mayer bond between sphere and needle, hence $-f_{SN} = w_3^S * w_0^N + w_2^{SN} * w_1^N$. This can be seen by considering the cases where the above expressions are nonvanishing: In Eq. (A2), the step function counts the number of needle endpoints that lie in the sphere. In Eq. (A4) the first step function is nonzero only if the needle axis intersects the sphere. If it does, the second step function counts how often the needle intersects the surface of the sphere. This covers all cases of sphere-needle overlap.

2. The rod-rod Mayer bond in the Onsager limit

Since only the relative orientation of both rods is relevant, we take $\mathbf{\Omega}' = (0, 0, 1)$, $\mathbf{\Omega} = (0, \sin \theta, \cos \theta)$; the difference vector between both particle positions is (x, y, z) . We then perform the spatial convolution of the weight functions given in Eqs. (1), (14) as

$$-2w_2^{NN}(\mathbf{r}, \mathbf{\Omega}; \mathbf{\Omega}') * w_1^N(\mathbf{r}, \mathbf{\Omega}') \quad (\text{A5})$$

$$= -2D \int_{-\infty}^{\infty} dz' \int_{-\infty}^{\infty} dy' \int_{-\infty}^{\infty} dx' \sin \theta \int_{-L/2}^{L/2} dl \delta(x') \delta(y' + l \sin \theta) \delta(z' + l \cos \theta) \\ \times \int_{-L/2}^{L/2} dl' \delta(x - x') \delta(y - y') \delta(z - z' + l') \quad (\text{A6})$$

$$= -2D \int_{-\infty}^{\infty} dz' \int_{-\infty}^{\infty} dy' \int_{-\infty}^{\infty} dx' \tan \theta \delta(x') \Theta\left(\frac{L}{2} - \left| \frac{y'}{\sin \theta} \right|\right) \delta\left(z' - \frac{y'}{\tan \theta}\right) \\ \times \int_{-L/2}^{L/2} dl' \delta(x - x') \delta(y - y') \delta(z - z' + l') \quad (\text{A7})$$

$$= -2D \delta(x) \Theta\left(\frac{L}{2} - \left| \frac{y}{\tan \theta} + z \right|\right) \Theta\left(\frac{L}{2} - \left| \frac{y}{\sin \theta} \right|\right) \quad (\text{A8})$$

$$= f_{NN}(\mathbf{r}, \mathbf{\Omega}; \mathbf{\Omega}'). \quad (\text{A9})$$

From Eq. (A6) to (A7), we solve the integral over l as an explanatory case; the other integrals can be done analogously. In order to recognize that Eq. (A8) is indeed the rod-rod Mayer bond, we compare with the expressions given in Ref. [43], and observe that the step-functions in Eq. (A8) correspond to Eqs. (A1), (A2) in the Appendix of Ref. [43]. Since $\lim_{D \rightarrow 0} \Theta(D - |x|)/(2D) = \delta(x)$, the term $2D \delta(x)$ corresponds to Eq. (A3) in Ref. [43] in the limit of small values of D , hence Eq. (A9) constitutes a valid equality.

APPENDIX B: WEIGHT FUNCTIONS IN PLANAR GEOMETRY

The reduced weight functions in planar geometry appearing in Eqs. (18)–(20) are obtained as

$$w_v^N(z, \theta) = \int_{-\infty}^{\infty} dx \int_{-\infty}^{\infty} dy w_v^N(\mathbf{r}, \mathbf{\Omega}), \quad (\text{B1})$$

$$w_v^S(z) = \int_{-\infty}^{\infty} dx \int_{-\infty}^{\infty} dy w_v^S(\mathbf{r}), \quad (\text{B2})$$

$$w_2^{SN}(z, \theta) = \int_{-\infty}^{\infty} dx \int_{-\infty}^{\infty} dy w_2^{SN}(\mathbf{r}, \mathbf{\Omega}), \quad (\text{B3})$$

where $\mathbf{r} = (x, y, z)$, and in the following we employ cylindrical coordinates $\mathbf{r} = (r \cos \varphi, r \sin \varphi, z)$. For the scalar and vectorial sphere weight functions [Eqs. (3), (4)] as well as for the pure needle weight functions [Eqs. (1), (2)] the integrations in Eqs. (B1), (B2) are straightforward and yield the results given in Eqs. (22)–(26). The calculations for $\hat{w}_{m2}^S(z)$ and $w_2^{SN}(z, \theta)$ [defined through Eqs. (4), (5), respectively] are slightly more involved, and are given explicitly in the following sections.

1. Tensor sphere weight function

We insert the definition of the tensor weight [Eq. (4)] into Eq. (B2),

$$\hat{w}_{m2}^S(z) = \int_{-\infty}^{\infty} dx \int_{-\infty}^{\infty} dy \delta(R - |\mathbf{r}|) \left(\frac{\mathbf{r}\mathbf{r}}{r^2} - \frac{\hat{\mathbf{1}}}{3} \right) \quad (\text{B4})$$

$$= \int_0^{2\pi} d\varphi \int_0^{\infty} dr r \delta(R - \sqrt{r^2 + z^2}) \left[(r^2 + z^2)^{-1} \begin{pmatrix} r^2 \sin^2 \varphi & r^2 \sin \varphi \cos \varphi & r \sin \varphi z \\ r^2 \sin \varphi \cos \varphi & r^2 \cos^2 \varphi & r \cos \varphi z \\ r \sin \varphi z & r \cos \varphi z & z^2 \end{pmatrix} - \frac{\hat{\mathbf{1}}}{3} \right] \quad (\text{B5})$$

$$= \int_0^{\infty} dr r \delta(R - \sqrt{r^2 + z^2}) \left((r^2 + z^2)^{-1} \text{diag}(\pi r^2, \pi r^2, 2z^2) - \frac{2\pi}{3} \hat{\mathbf{1}} \right) \quad (\text{B6})$$

$$= \left(\frac{\pi}{R} \text{diag}(R^2 - z^2, R^2 - z^2, 2z^2) - \frac{2\pi R}{3} \hat{\mathbf{1}} \right) \Theta(R^2 - z^2), \quad (\text{B7})$$

from which Eq. (27) can be readily obtained. The off-diagonal elements in Eq. (B5) vanish due to the φ integration over a complete wavelength, and to obtain Eq. (B7) we have used $\delta[f(x)] = |f'(x_0)|^{-1} \delta(x - x_0)$, where x_0 is the zero of $f(x)$, hence $f(x_0) = 0$.

2. Mixed sphere-needle weight function

Due to the rotational symmetry around the z axis, we can take $\mathbf{\Omega} = (\sin \theta, 0, \cos \theta)$, and due to the inflection symmetry of the needles, we can restrict to $0 \leq \theta \leq \pi/2$. By inserting the definition of the mixed weight function [Eq. (5)] into Eq. (B3) we obtain

$$w_2^{SN}(z, \theta) = 2 \int dx \int dy \left| \delta(R - |\mathbf{r}|) \frac{1}{\sqrt{r^2 + z^2}} \begin{pmatrix} r \cos \varphi \\ r \sin \varphi \\ z \end{pmatrix} \cdot \begin{pmatrix} \sin \theta \\ 0 \\ \cos \theta \end{pmatrix} \right| \quad (\text{B8})$$

$$= 2 \int_0^{2\pi} d\varphi \int_0^{\infty} dr r \left| \delta(R - \sqrt{r^2 + z^2}) \frac{z \cos \theta + r \cos \varphi \sin \theta}{\sqrt{r^2 + z^2}} \right| \quad (\text{B9})$$

$$= \left\{ \left[8\sqrt{(R^2-z^2)\sin^2\theta - z^2\cos^2\theta} + 4z\cos\theta\operatorname{sgn}(\sqrt{R^2-z^2}\sin\theta) \right. \right. \\ \left. \left. \times \arcsin\left(\frac{z\cos\theta}{\sqrt{R^2-z^2}\sin\theta}\right) \right] \Theta\left(1 - \left|\frac{z\cos\theta}{\sqrt{R^2-z^2}\sin\theta}\right|\right) + 4\pi|z\cos\theta|\Theta\left(\left|\frac{z\cos\theta}{\sqrt{R^2-z^2}\sin\theta}\right| - 1\right) \right\} \Theta(R-|z|) \quad (\text{B10})$$

$$= \begin{cases} 8\sqrt{R^2\sin^2\theta - z^2} + 8z\cos\theta\arcsin\left(\frac{z\cot\theta}{\sqrt{R^2-z^2}}\right) & \text{if } |z| < R\sin\theta, \\ 4\pi|z|\cos\theta & \text{if } R\sin\theta \leq |z| \leq R, \\ 0 & \text{otherwise.} \end{cases} \quad (\text{B11})$$

In Eq. (B9), we have used the same representation for the δ function as before. The nontrivial part is the integral over φ , which we discuss in the following. It is of the form

$$\int_0^{2\pi} |a + b\cos\varphi| d\varphi \quad (\text{B12})$$

with constants (with respect to φ) a, b . Due to the symmetry of the cosine function, the integration from 0 to π gives the same result as that from π to 2π . We consider two cases: The argument of $|\cdot|$ changes its sign once if $|a/b| < 1$, and we have

$$\int_0^\pi |a + b\cos\varphi| d\varphi \quad (\text{B13}) \\ = \operatorname{sgn}(a+b)([a\varphi + b\sin\varphi]_0^x + [-a\varphi - b\sin\varphi]_x^\pi) \quad (\text{B14})$$

$$= \operatorname{sgn}(b)(2b\sin x + 2ax - a\pi) \quad (\text{B15})$$

$$= \operatorname{sgn}(b)\left(2b\sin\arccos\frac{-a}{b} + 2a\arccos\frac{-a}{b} - a\pi\right) \quad (\text{B16})$$

$$= 2\sqrt{b^2 - a^2} + 2a\operatorname{sgn}(b)\arcsin\frac{a}{b}, \quad (\text{B17})$$

where $x = \arccos(-a/b)$. If, on the other hand, $|a/b| > 1$, the argument does not change its sign. Then, $|a + b\cos\varphi| = (a + b\cos\varphi)\operatorname{sgn}(a)$,

$$\int_0^\pi |a + b\cos\varphi| d\varphi = |a|\pi. \quad (\text{B18})$$

Note that in Eq. (B10), $\operatorname{sgn}(\cdot) = +1$ holds, since $0 \leq \theta \leq \pi/2$.

-
- [1] M. Adams, Z. Dogic, S.L. Keller, and S. Fraden, *Nature* (London) **393**, 349 (1998).
[2] G.A. Vliegthart and H.N.W. Lekkerkerker, *J. Chem. Phys.* **111**, 4153 (1999).
[3] G.H. Koenderink, G.A. Vliegthart, S.G.J.M. Kluijtmans, A. van Blaaderen, A.P. Philipse, and H.N.W. Lekkerkerker, *Langmuir* **15**, 4693 (2000).
[4] K. Lin, J.C. Crocker, A.C. Zeri, and A.G. Yodh, *Phys. Rev. Lett.* **87**, 088301 (2001).
[5] M. Elbaum, D.K. Fygenon, and A. Libchaber, *Phys. Rev. Lett.* **76**, 4078 (1996).
[6] D.K. Fygenon, M. Elbaum, B. Shraiman, and A. Libchaber, *Phys. Rev. E* **55**, 850 (1997).
[7] S.G.J.M. Kluijtmans, G.H. Koenderink, and A.P. Philipse, *Phys. Rev. E* **61**, 626 (2000).
[8] G. A. Vliegthart, Dissertation, Utrecht University, 1999.
[9] P. Bolhuis and D. Frenkel, *J. Chem. Phys.* **101**, 9869 (1994).
[10] S. Asakura and F. Oosawa, *J. Chem. Phys.* **22**, 1255 (1954).
[11] A. Vrij, *Pure Appl. Chem.* **48**, 471 (1976).
[12] H.N.W. Lekkerkerker, W.C.K. Poon, P.N. Pusey, A. Stroobants, and P.B. Warren, *Europhys. Lett.* **20**, 559 (1992).
[13] K. Yaman, C. Jeppesen, and C.M. Marques, *Europhys. Lett.* **42**, 221 (1998).
[14] Y. Mao, M.E. Cates, and H.N.W. Lekkerkerker, *Phys. Rev. Lett.* **75**, 4548 (1995).
[15] Y. Mao, M.E. Cates, and H.N.W. Lekkerkerker, *J. Chem. Phys.* **106**, 3721 (1997).
[16] Z. Dogic, D. Frenkel, and S. Fraden, *Phys. Rev. E* **62**, 3925 (2000).
[17] R. Evans, in *Fundamentals of Inhomogeneous Fluids*, edited by D. Henderson (Dekker, New York, 1992), p. 85.
[18] R. Evans, *Adv. Phys.* **28**, 143 (1979).
[19] Y. Rosenfeld, *Phys. Rev. Lett.* **63**, 980 (1989).
[20] Y. Rosenfeld, M. Schmidt, H. Löwen, and P. Tarazona, *J. Phys.: Condens. Matter* **8**, L577 (1996).
[21] Y. Rosenfeld, M. Schmidt, H. Löwen, and P. Tarazona, *Phys. Rev. E* **55**, 4245 (1997).
[22] P. Tarazona and Y. Rosenfeld, *Phys. Rev. E* **55**, R4873 (1997).
[23] P. Tarazona, *Phys. Rev. Lett.* **84**, 694 (2000).
[24] Y. Rosenfeld, *Phys. Rev. E* **50**, R3318 (1994).
[25] A. Chamoux and A. Perera, *J. Chem. Phys.* **104**, 1493 (1996).
[26] A. Chamoux and A. Perera, *Phys. Rev. E* **58**, 1933 (1998).

- [27] A. Chamoux and A. Perera, *Mol. Phys.* **93**, 649 (1998).
[28] M. Schmidt, *Phys. Rev. E* **63**, 050201(R) (2001).
[29] M. Schmidt and C. von Ferber, *Phys. Rev. E* **64**, 051115 (2001).
[30] M. Schmidt and A.R. Denton, *Phys. Rev. E* **65**, 021508 (2002).
[31] R. Roth, R. van Roij, D. Andrienko, K. R. Mecke, and S. Dietrich, *Phys. Rev. Lett.* (in press), eprint cond-mat/0202443.
[32] K. Shundyak and R. van Roij, *J. Phys.: Condens. Matter* **13**, 4789 (2001), and references therein.
[33] M.E. Fisher and B. Widom, *J. Chem. Phys.* **50**, 3756 (1969).
[34] R. Evans, J.R. Henderson, D.C. Hoyle, A.O. Parry, and Z.A. Sabeur, *Mol. Phys.* **80**, 755 (1993).
[35] R. Evans, R.J.F. Leote de Carvalho, J.R. Henderson, and D.C. Hoyle, *J. Chem. Phys.* **100**, 591 (1994).
[36] M. Dijkstra and R. Evans, *J. Chem. Phys.* **112**, 1449 (2000).
[37] J.M. Brader, R. Evans, M. Schmidt, and H. Löwen, *J. Phys.: Condens. Matter* **14**, L1 (2002).
[38] J.M. Brader, M. Dijkstra, and R. Evans, *Phys. Rev. E* **63**, 041405 (2001).
[39] L. Onsager, *Ann. N.Y. Acad. Sci.* **51**, 627 (1949).
[40] J.A. Barker and D. Henderson, *Rev. Mod. Phys.* **48**, 587 (1976).
[41] R. van Roij, M. Dijkstra, and R. Evans, *Europhys. Lett.* **49**, 350 (2000).
[42] A.J. Archer and R. Evans, *Phys. Rev. E* **64**, 041501 (2001).
[43] H. Löwen, *Phys. Rev. E* **50**, 1232 (1994).